MMSE Beam Forming on Fast-Scanning Phased Array Weather Radar

Eiichi Yoshikawa, Tomoo Ushio, Zen Kawasaki, Satoru Yoshida, Takeshi Morimoto, Fumihiko Mizutani, and Masakazu Wada, *Member, IEEE*

***Abstract*—A fast-scanning phased array weather radar (PAWR) with a digital beam forming receiver is under development. It is important in beam forming for weather radar observation with temporally high resolution to form a stable and robust mainlobe and adaptively suppress sidelobes with a small number of pulses in order to accurately estimate precipitation profiles (reflectivity, mean Doppler velocity, and spectral width). A minimum mean-square error (MMSE) formulation with a power constraint, proposed in this paper, gives us adaptively formed beams that satisfy these demands. The MMSE beam-forming method is compared in various precipitation radar signal simulations with traditional beam-forming methods, Fourier and Capon methods, which have been applied in atmospheric research to observe distributed targets such as precipitation, and it is shown that the MMSE method is appropriate to this fast-scanning PAWR concept.**

***Index Terms*—Phased array digital beam forming, distributed targets, fast-scanning weather radar**

I. Introduction

In the quest to rapidly detect hazardous weather phenomena and provide warning information, a weather radar system using a phased array antenna system that achieves high speed scans has been attracting attention. The Collaborative Adaptive Sensing of Atmosphere (CASA) project has proposed a phased array radar network to efficiently observe precipitation by electronic scan, steering beams for weather phenomena adaptively [1], [2]. In [3], a multi-function phased array radar for not only detecting weather phenomena but controlling air traffic and tracking non-cooperative airplanes by using a rapid scan has been proposed. For the fast scanning purpose, CASA IP1 radar, Rapid-Scan DOW, Atmospheric Imaging Radar, RaxPol, MWR-05XP, and so on has been proposed and developed [4], [5], [6], [7], [8].

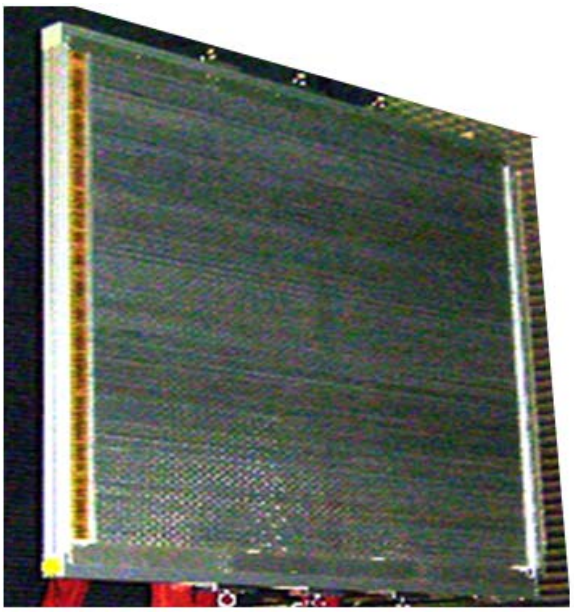

Fig. 1. Antenna array of PAWR. 128 slotted waveguide antennas are aligned vertically for rapid scanning.

At present we are developing a phased array weather radar (PAWR) to rapidly scan in 3-D and finely detect hazardous weather phenomena such as tornadoes and downbursts with a lifetime below 60 min and horizontal scale on the order of 100 m. 1-D array antenna (horizontal polarization) consisting of 128 elements for elevation is installed in the PAWR, as shown in Fig. 1. A fan beam is transmitted via feeding power (430 W) into 12 to 24 elements. After receiving and sampling scattered signals with all 128 elements into 128 analog-to-digital converters (ADC; 14 bits, 48 MHz), adaptive digital beam forming (DBF) is performed to sharpen the fan beam. Thus, precipitation at several elevation angles is simultaneously observed and temporal resolution is drastically improved. Although the PAWR is under development and many specifications are not fixed, the transmitting fan and receiving sharp beam widths are expected as 10 and 1 deg, respectively, for elevation, which achieves a 500 m 3-D mesh with a sensitivity of 18 dBZ (equivalent to about 0.5 mm/h) at the maximum range of about 25 km and 10 sec per volume scan while transmitting around 16 pulses for a direction. Other

Manuscript received January 10, 2012. This work is supported by Toshiba Corporation and the National Institute of Information and Communications Technology (NICT).

Eiichi Yoshikawa was with Osaka University, Osaka, Japan and Colorado State University, CO, USA, and now is with Japan Aerospace Exploration Agency (JAXA), Tokyo, Japan (phone: +81-(0)50-3362-3797; e-mail: yoshikawa.eiichi@jaxa.jp).

Tomoo Ushio is with Osaka University, Osaka, Japan.

Zen Kawasaki is with Osaka University, Osaka, Japan and Egypt-Japan University of Science and Technology (E-JUST), Alexandria, Egypt.

Satoru Yoshida is with Osaka University, Osaka, Japan.

Takeshi Morimoto was with Osaka University, Osaka, Japan, and now is with Kinki University, Osaka, Japan.

Fumihiko Mizutani and Masakazu Wada are with Toshiba Corporation, Tokyo, Japan.

details of the PAWR have been presented in [9] (These parameters may change in the future).

A significant problem with fan beam transmission is huge sidelobes of strong echoes from strong precipitation cells or clutter, which are almost two times stronger than a sharp beam transmission and reception in dB. For example, while a sharp beam transmission and reception has a first sidelobe level of -26 dB from the main lobe for the center direction, a configuration of uniform and sharp beams has a first sidelobe level of -13 dB in the same angle. Many adaptive DBF methods have been proposed to achieve sidelobe reduction in a phased array antenna system. In atmospheric radars observing a scattering volume filled with particles, the Capon method has been used [10], [11], [12], [13], [14], [15] for both beam forming and ranging. The Capon approach requires a sufficient number of samples (pulses) to estimate accurately and cannot work well with 16 pulses in the PAWR. Alternatively, a direction-of-arrival (DOA) approach for point targets based on the minimum mean-square error (MMSE) framework has been proposed [16]. This approach does not employ spatial sample covariance information, which degrades DOA estimation in the Capon or some other DOA methods in cases where correlated signals are scattered in different directions, on the prior assumption that they are uncorrelated. Therefore, the number of pulses is not essential in this framework. In this paper, a modified MMSE approach for sidelobe reduction and accurate estimation for distributed targets with fewer pulses on the PAWR is proposed and evaluated. For meteorological application, not only DOA but also estimation of received power and shifted phase from distributed targets is important, which derive physical parameters of precipitation. By the modifications, gain constraint and convergence criteria, these received power and phase are correctly estimated.

This paper is organized as follows. In Section II, the signal model of phased array radar and the MMSE algorithm are elaborated. Two traditional methods, Fourier and Capon beam forming, are introduced and are used for performance comparisons in the following sections. In Section III, estimation accuracies of these three methods are evaluated and compared with the use of numerical simulations, in which signals are generated by a precipitation radar signal simulator. In Section IV, estimation results for precipitation are described with the use of measurements from the CSU-CHILL radar.

II. METHODOLOGY

A. Signal Model

Assuming that a linear-spaced phased array antenna with N antenna elements, l th time sample of a received complex amplitude $\mathbf{y}_l$ (N-vector) is expressed by an associated complex amplitude $\mathbf{x}_l$ ($M\times 1$-vector, $M \gg N$) in an arbitrary range bin, an $N\times M$-vector $\mathbf{S}$ which consists of spatial steering vector $\mathbf{s}(\theta)$, and an additional Gaussian noise vector $\mathbf{v}_l$ as

$$\mathbf{y}_l = \mathbf{S}\mathbf{x}_l + \mathbf{v}_l , \tag{1}$$

where

$$\mathbf{y}_l = \begin{bmatrix} y_{l,0} & y_{l,1} & \cdots & y_{l,N-1} \end{bmatrix}^T , \tag{2}$$

$$\mathbf{x}_l = \begin{bmatrix} x_{l,0} & x_{l,1} & \cdots & x_{l,M-1} \end{bmatrix}^T , \tag{3}$$

$$\mathbf{S} = \begin{bmatrix} \mathbf{s}(\theta_0) & \mathbf{s}(\theta_1) & \cdots & \mathbf{s}(\theta_{M-1}) \end{bmatrix}, \tag{4}$$

$$\mathbf{s}(\theta) = \begin{bmatrix} 1 & \exp(-j\omega_1(\theta)) & \cdots & \exp(-j\omega_{N-1}(\theta)) \end{bmatrix}^T , \tag{5}$$

and

$$\omega_n(\theta) = (2\pi/\lambda) dn \sin\theta . \tag{6}$$

$[\bullet]^T$ is a transpose. λ is wavelength and d is spacing of neighboring antenna elements. In the PAWR, θ means elevation angle, and $\mathbf{x}$ corresponds to M-separated precipitation profiles in elevation angles.

In adaptive array signal processing, estimated precipitation profiles are calculated as

$$\hat{\mathbf{x}}_l = \begin{bmatrix} \hat{x}_{l,0} & \hat{x}_{l,1} & \cdots & \hat{x}_{l,M-1} \end{bmatrix}^T , \tag{7}$$

$$\hat{x}_{l,m} = \mathbf{w}_m^H \mathbf{y}_l , \tag{8}$$

where $\mathbf{w}$ is an N complex weighting vector for received complex amplitudes of each antenna element. $[\bullet]^H$ is a complex-conjugate transpose.

B. Fourier Beam Forming (FR)

Fourier beam forming (FR), also known as a matched filter, is the most basic method in phased array radars for steering a beam in a direction by uniform phase shift. In FR, the weighting complex vector (FR weight) is expressed as

$$\mathbf{w}_{\mathrm{FR}\,m} = \mathbf{s}(\theta_m)/N . \tag{9}$$

Thus, a precipitation profile estimated by using FR weight is equivalent to the result of a Fourier transform of $\mathbf{y}_l$.

C. Capon Beam Forming (CP)

The Capon beam-forming method (CP) minimizes received power subject to a constraint in which a desired direction is constant [10], [11], [12], [13], [14], [15]. In CP, weighting complex vector is expressed as

$$\mathbf{w}_{\mathrm{CP}\,m} = \frac{\mathbf{R}_y^{-1}\mathbf{s}(\theta_m)}{\mathbf{s}^H(\theta_m)\mathbf{R}_y^{-1}\mathbf{s}(\theta_m)}, \tag{10}$$

where

$$\mathbf{R}_y = \frac{1}{L}\sum_{l=1}^{L} \mathbf{y}_l \mathbf{y}_l^H . \tag{11}$$

L is the number of time samples.

D. MMSE Beam Forming

MMSE beam forming for adaptive phased array was proposed in [16], it is based on the same concept as an adaptive pulse compression (APC) algorithm [17], [18], [19]. To estimate received power accurately, we apply a concept of gain-constrained APC [20], whose constrained cost function is

$$J_m = E\left[\left| x_m - \mathbf{w}_{\mathrm{MMSE}\,m}^H \mathbf{y} \right|^2\right] + \mathrm{Re}\left\{\lambda\left(\mathbf{w}_{\mathbf{MMSE}\,m}^H \mathbf{s}(\theta_m) - 1\right)\right\} , \tag{12}$$

where $E[\bullet]$ is expectation, $\mathrm{Re}\{\bullet\}$ is the real part, and λ is a

Lagrange multiplier. Minimizing Eq. (12), the weighting complex vector of MMSE beam forming (MMSE weight) is expressed as

$$\mathbf{w}_{\mathrm{MMSE}\,m} = \frac{\mathbf{R}^{-1}\mathbf{s}(\theta_m)}{\mathbf{s}^H(\theta_m)\mathbf{R}^{-1}\mathbf{s}(\theta_m)}, \quad (13)$$

where

$$\mathbf{R} = \mathbf{S}\mathbf{R}_x\mathbf{S}^H + \mathbf{R}_v. \quad (14)$$

$\mathbf{R}_x$ is a covariance matrix of $\mathbf{x}$ as

$$\mathbf{R}_x = E\left[\mathbf{x}\mathbf{x}^H\right] \approx \left[\frac{1}{L}\sum_{l=1}^{L}\mathbf{x}_l\mathbf{x}_l^H\right] \odot \mathbf{I}_{M\times M}. \quad (15)$$

$\odot$ is the Hadamard product and $\mathbf{I}_{M\times M}$ is an $M\times M$ identity matrix. Eq. (15) is based on the assumption that signal sources from different positions are temporally uncorrelated. $\mathbf{R}_v$ is a noise covariance matrix expressed as

$$\mathbf{R}_v = E\left[\mathbf{v}\mathbf{v}^H\right] \approx {\sigma_v}^2\mathbf{I}_{M\times M} \quad (16)$$

where σ_v^2 is variance of thermal noise, which is assumed as a white noise. Comparing Eqs. (14) and (15) to Eqs. (10) and (11), it is clear that the MMSE cost function with gain constraint reaches the same solution as CP. The advantages of MMSE beamforming is derived from a way to determine the covariance matrix as indicated in Eqs. (15) and (16), where an unknown vector $\mathbf{x}$ is included. MMSE weight and solution are calculated iteratively with the use of prior information as follows.

1) Prior Information

As prior information, the solution of FR is substituted in Eq. (15).

$$\mathbf{R}_x^{(0)} = \left[\frac{1}{L}\sum_{l=1}^{L}\hat{\mathbf{x}}_{\mathrm{FR}\,l}\hat{\mathbf{x}}_{\mathrm{FR}\,l}^H\right] \odot \mathbf{I}_{M\times M}, \quad (17)$$

where

$$\hat{\mathbf{x}}_{\mathrm{FR}\,l} = \left[\hat{x}_{\mathrm{FR}\,l,0} \quad \hat{x}_{\mathrm{FR}\,l,1} \quad \cdots \quad \hat{x}_{\mathrm{FR}\,l,M-1}\right]^T, \quad (18)$$

$$\hat{x}_{\mathrm{FR}\,l,m} = \mathbf{w}_{\mathrm{FR}\,m}^H\mathbf{y}_l. \quad (19)$$

L is the number of time samples as in CP method.

2) Determination of MMSE Weights

M MMSE weights are determined by i-iterative $\mathbf{R}_x$.

$$\mathbf{w}_{\mathrm{MMSE}\,m}^{(i)} = \frac{\mathbf{R}^{(i)^{-1}}\mathbf{s}(\theta_m)}{\mathbf{s}^H(\theta_m)\mathbf{R}^{(i)^{-1}}\mathbf{s}(\theta_m)}, \quad (20)$$

where

$$\mathbf{R}^{(i)} = \mathbf{S}\mathbf{R}_x^{(i)}\mathbf{S}^H + \mathbf{R}_v. \quad (21)$$

3) Computation of MMSE solutions

M MMSE solutions are calculated by i-iterative $\mathbf{w}_{\mathrm{MMSE}\,m}$.

$$\hat{\mathbf{x}}_{\mathrm{MMSE}\,l}^{(i)} = \left[\hat{x}_{\mathrm{MMSE}\,l,0}^{(i)} \quad \hat{x}_{\mathrm{MMSE}\,l,1}^{(i)} \quad \cdots \quad \hat{x}_{\mathrm{MMSE}\,l,M-1}^{(i)}\right]^T, \quad (22)$$

where

$$\hat{x}_{\mathrm{MMSE}\,l,m}^{(i)} = \mathbf{w}_{\mathrm{MMSE}\,m}^{(i)H}\mathbf{y}_l. \quad (23)$$

4) Re-iteration

$i+1$-iterative $\mathbf{R}_x$ is calculated by i-iterative MMSE solutions.

$$\mathbf{R}_x\big|_{i+1} = \left[\frac{1}{L}\sum_{l=1}^{L}\hat{\mathbf{x}}_{\mathrm{MMSE}\,l}^{(i)}\hat{\mathbf{x}}_{\mathrm{MMSE}\,l}^{(i)H}\right] \odot \mathbf{I}_{M\times M}, \quad (24)$$

And then, return to 2).

In this paper, the iteration is terminated with a threshold of normalized mean square errors (NMSE) between i-iterative and i-1-iterative MMSE solutions,

$$\delta_i = \frac{1}{M}\sum_{m=1}^{M}\left(\frac{\sum_{l=1}^{L}\left\|\hat{x}_{\mathrm{MMSE}\,l,m}^{(i)} - \hat{x}_{\mathrm{MMSE}\,l,m}^{(i-1)}\right\|^2}{\sum_{l=1}^{L}\left\|\hat{x}_{\mathrm{MMSE}\,l,m}^{(i-1)}\right\|^2}\right), \quad (25)$$

where NMSEs in each range bin are averaged. Hereafter, an i-iterative MMSE is called MMSE(i), and, if it satisfies Eq. (25), it is called cMMSE(i) as a converged result.

TABLE I
CHARACTERISTICS OF NUMERICAL SIMULATION

Parameter	Value
frequency	9.4 GHz
number of antenna elements (N)	128
spacing of neighboring antenna elements (d)	16.5 mm
tilt angle of antenna	30 deg
pulse repetition frequency	5.4 kHz
number of pulses (L)	16 and 256
number of associated elevation angles (M)	1201 (every 0.1 deg from -30 to 90 deg)
convergence criteria	$\delta_i < 0.001$ or 20th iteration count

III. NUMERICAL SIMULATIONS

To evaluate the performance of MMSE beam forming and to compare it with other traditional beam-forming methods, radar signal simulations were carried out. The simulation signals were generated by a procedure described by Chandrasekar et al. [21] that generates a time series of received signals having a Gaussian spectral shape with window effect and randomness (see also [22]). Elevation profiles of power, mean radial velocity, and spectral width, which are corresponding to $\mathbf{x}$, are determined in each simulation model. Then, received signals, $\mathbf{y}$, are calculated as Eq. (1) with thermal noise (noise levels are also determined arbitrarily in each model). Here, each antenna element is assumed as omnidirectional. Characteristics of this simulation are shown in Table I. Frequency, the number of antenna elements, interval of neighboring antenna elements, tilt angle of antenna, and pulse repetition frequency are designed parameters of PAWR (they may change because the system is under development). Although 256 pulse samples would not be transmitted in the PAWR observation, this simulation is carried out to make a comparison with CP, which is not appropriate with a small number of pulses. A wide range of elevations from -30 to 90 deg is considered. Since the PAWR transmits a fan

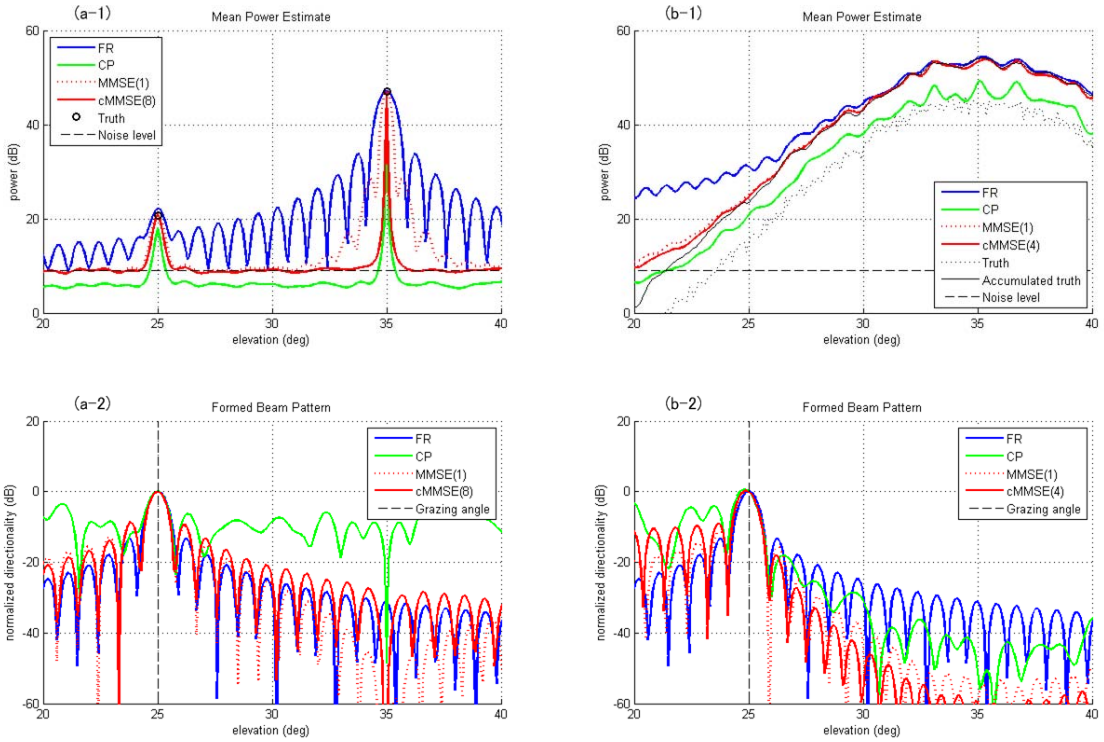

Fig. 2. Examples of mean power estimates and formed beam patterns for two-point targets and distributed targets. Panel (a-1) shows the mean power estimates for two targets placed at elevations of 25 and 5 deg, respectively, in which blue solid, green solid, red dotted, and red solid lines indicate results of FR, CP, MMSE(1), and cMMSE, respectively. Black circles and a dashed line indicate truth and given noise level. In Panel (a-2), a formed beam pattern grazing at an elevation angle of 25 deg (indicated by a black dashed line) in the case with the two point targets are shown, in which four colored lines indicate each method, as Panel (a-1). In Panels (b-1) and (b-2), respectively, those for the distributed targets are shown. A black solid line in Panel (b-1) is accumulated truth, which is derived from convolution between truth and the mainlobe of FR.

beam with -3-dB beam width of about 10 deg, we may deal with a narrower range of elevation, which gives us less computational cost. However, the fan beam is not considered here because these beam-forming methods are signal processing only for the receiver side and are independent on transmission. Additionally, the simulation with this wide range of elevation obviously shows the differences in these methods. The threshold of δ_i for convergence of MMSE is set to below 0.001 (-30 dB). Even if it does not satisfy the standard, the algorithm is terminated in the 20th iteration.

A. Point Targets and Distributed Targets

The Capon and MMSE methods were originally designed for detection of point targets such as aircraft. It is important to understand the differences in their performance for distributed targets such as precipitation. In Panels (a-1) of Fig. 2, an example of mean power estimates for two point targets is shown. It is assumed that the two targets are placed at elevations of 25 and 35 deg, respectively, in the same range and azimuth bin with mean received power of 20 and 50 dB, mean Doppler velocities of 8 and 10 m/sec, and spectral widths of 1 m/sec, as indicated by the black circles. The mean power of additional white noise is assumed to about 10 dB as indicated by the black dashed line. To show the results of CP, 256 pulses are given. The blue, green solid, red dot, and red solid lines are FR, CP, MMSE(1), and cMMSE, respectively. The estimated results of the two elevations are summarized in Table II (the truths do not strictly agree with the input parameters indicated above because the radar signal simulator gives randomness). FR correctly estimates the received power of the right (strong) target; however, it has the poorest resolution and highest sidelobes. The left (weak) target is almost hidden and its received power is overestimated by about 2.4 dB by sidelobes of the right (strong) target. Although the CP correctly detects both targets with high resolution and sufficiently suppresses sidelobes under the noise level, both received powers are underestimated, with 2.7 and 3.1 dB for the left and right targets, respectively. This underestimation is caused by a correlation between both the signals (it is well known that CP works when received signals are independent). Therefore, this problem is resolved with the use of more pulses. cMMSE shows high resolution and low sidelobes equivalent to CP and

TABLE II
MEAN POWER ESTIMATES FOR THE POINT TARGETS

Algorithm	For the Left Target (dB)	For the Right Target (dB)
FR	23.19	50.59
CP	18.16	47.40
MMSE(1)	21.15	50.57
cMMSE	21.10	50.59
Truth	20.81	50.59

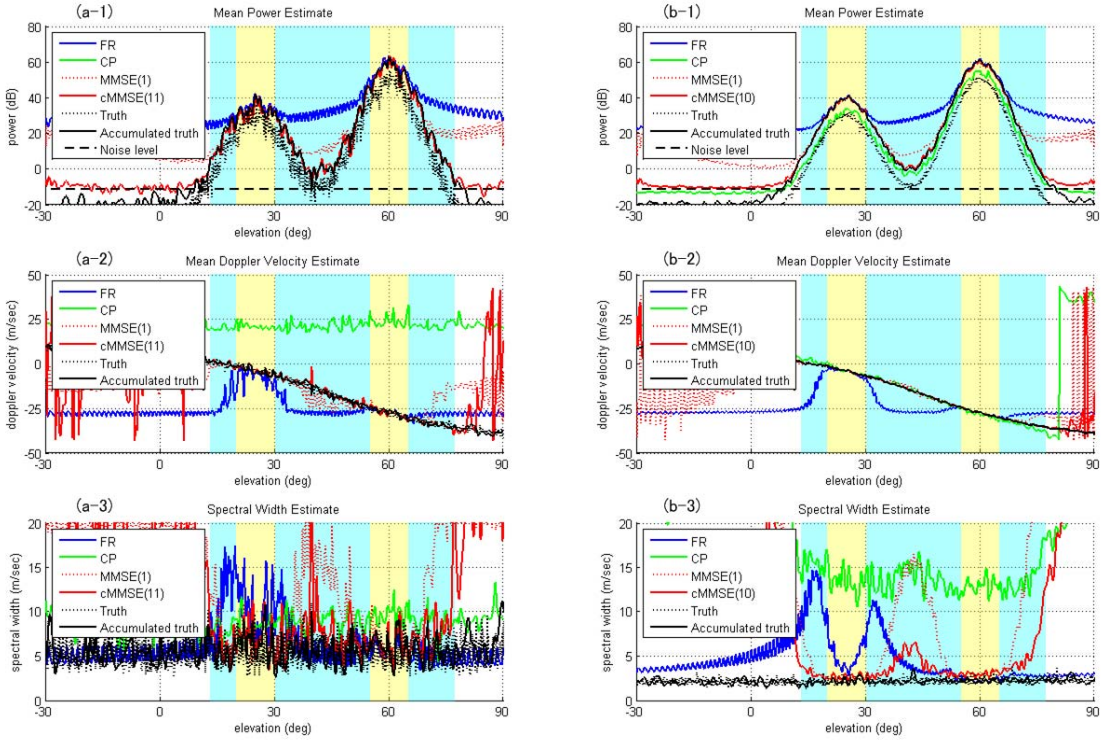

Fig. 3. Examples of mean power, mean Doppler velocity, and spectral width estimates calculated with 16 and 256 pulses. Those with 16 pulses are shown in Panels (a-1), (a-2), and (a-3), and those with 256 pulses are shown in Panels (b-1), (b-2), and (b-3), respectively. Blue solid, green solid, red dotted, red solid, black dotted, black solid, and black dashed lines are FR, CP, MMSE(1), cMMSE, truth, accumulated truth, and noise level, as in Fig. 1.

the best power estimation results for both the targets. A loss of signal-to-noise ratio (SNR) is also not seen. It is shown that the MMSE solutions converge step by step through FR, MMSE(1) to cMMSE(8). In Panel (a-2), formed beam patterns of each method for an elevation of 25 deg are shown. CP and cMMSE form a null at an elevation of 35 deg. That is why detection and power estimates of the left target are not affected by the right target in these methods. In contrast to Panel (a-1), in which resolution of CP and cMMSE(8) look very sharp, it is shown that their beam widths are almost equivalent to FR. This means that these beam-forming methods never sharpen mainlobes, which are essentially determined by antenna size, and only suppress sidelobes adaptively.

In Panel (b-1), an example of mean power estimates for distributed targets is shown. Also, the mean power of additional white noise is assumed to about 10 dB as indicated by the black dashed line. FR shows sidelobes below an elevation of 27 deg, and a correct shape of distributed targets with about +9 dB offset from the truth (corresponding absolute square of **x**) beyond the elevation, which is caused by a convolution between a formed beam pattern and the truth. Accumulated truth, which is calculated by a convolution of mainlobes of FR and distributed target, agrees with FR beyond 27 deg elevation. Although CP suppresses the sidelobes that FR has below 27 deg elevation, it underestimates caused by correlations between signals mean power in all elevations. Though the CP solutions get closer to the accumulated truth with more pulses as in the point-target simulation, this characteristic of CP is a serious problem for precipitation radars because the distributed targets change continuously, and a correlation between narrow-band random signals with similar frequencies is high. Compared with these methods, cMMSE correctly estimates mean power without underestimation, sidelobes, and loss of SNR. As shown in Panel (b-2), CP and cMMSE suppress sidelobes adaptively and mainlobes are not sharpened for distributed targets as in the point-target simulation. For distributed targets, these beam-forming methods estimate an accumulated mean power with weights of their mainlobes different from those for point targets, and this is completely consistent with the theory of radar equation for distributed targets.

B. Estimation Accuracy for Distributed Targets

Estimation accuracies of these methods are compared in three parameters—mean power, mean Doppler velocity, and spectral width—by a radar signal simulation assuming distributed targets with two precipitation cells. Examples of mean power, mean Doppler velocity, and spectral width estimates with 16 and 256 pulses are shown in Fig. 3. Here, the mean power of additional white noise is assumed to about -10 dB as indicated by the black dashed line as in Panels (a-1) and (b-1). Mean power, mean Doppler velocity, and spectral width estimates of these methods and accumulated truth are calculated with the use of the most general methods based on a time series, which is elaborated in Chapter 5 (5.10 and 5.11) of [23]. In Panels (a-1) and (b-1), FR shows high sidelobes in

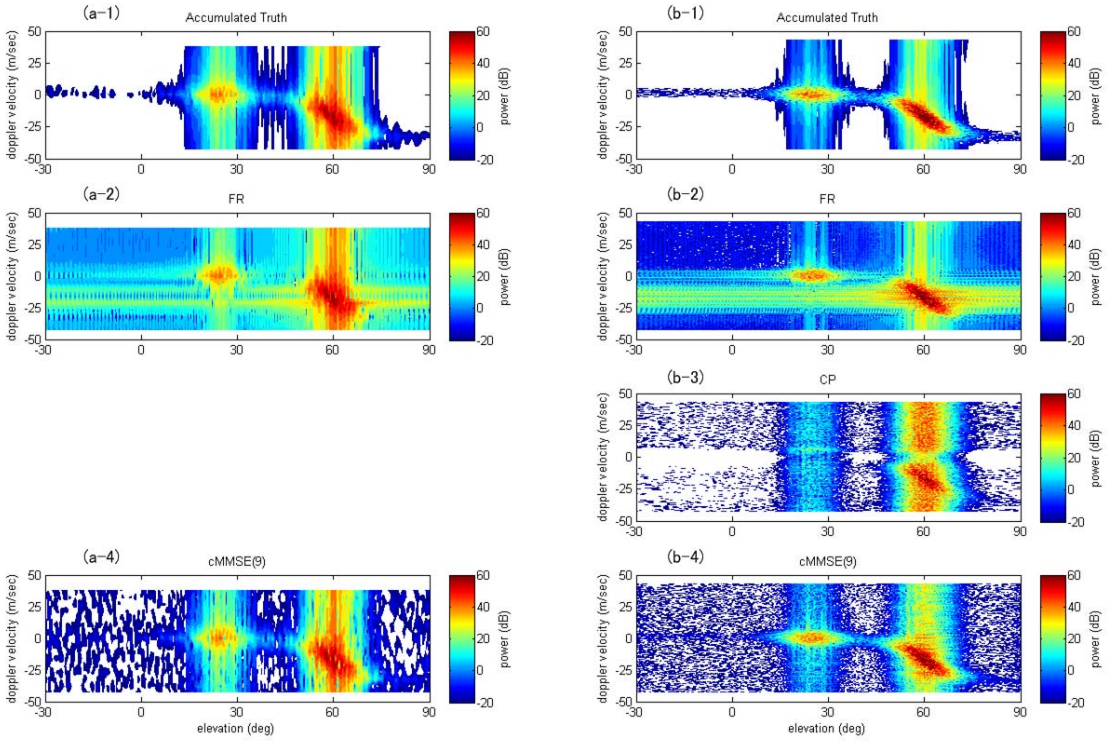

Fig. 4. Examples of elevation – Doppler velocity spectrographs at 16 and 256 pulses. In Panels (a-1), (a-2) and (a-4), spectrographs of accumulated truth, FR, and cMMSE are shown. Spectrograph of CP, corresponding to Panel (a-3), is not shown because of the over large underestimation with 16 pulses. Those of accumulated truth, FR, CP, and cMMSE with 256 pulses are shown in Panel (b-1), (b-2), (b-3), and (b-4), respectively.

mean power estimates, and correctly estimates them only in two yellow colored areas in elevations from 20 to 30 or from 55 to 65 deg, in which strong distributed targets exist. As mean power, Panels (a-2) and (b-2) show that mean Doppler velocity estimates of FR are close to accumulated truth in the yellow colored areas. Spectral widths of FR are correctly estimated only in the right yellow colored area as shown in Panels (a-3) and (b-3). It seems that the number of pulses is almost independent of estimated accuracies of FR. There is an obvious difference between CPs with 16 and 256 pulses. In Panels (a-1), CP has too large underestimations and is not described in the plot range. Therefore, estimated mean Doppler velocities and spectral widths in Panels (a-2) and (a-3), respectively, are likely meaningless. As shown in Panels (b-1), (b-2), and (b-3), CP results are better with a larger number of pulses. However, underestimations still remain. cMMSE has good results, as in previous simulations, regardless of the number of pulses. Since received power from targets are much smaller than the additional white noise in elevations below 10 or above 70 deg, spectral widths of cMMSE are very large, which corresponds to spectral width of white noise. Throughout Panels in Fig. 3, cMMSE's performance is obviously superior.

A quantitative evaluation of estimate accuracies applies to two regions of elevation; 1) beyond additive noise level in

TABLE III
ESTIMATION ACCURACIES

		beyond additive noise level in elevations from 13 to 77 deg (blue colored area)				beyond additive noise level in elevations from 20 to 30 and 55 to 65 deg (yellow colored areas)			
		L = 16		L = 256		L = 16		L = 256	
		mean bias	Standard deviation	mean bias	Standard deviation	mean bias	Standard deviation	mean bias	Standard deviation
FR	mean power (dB)	10.98	11.40	10.63	10.95	0.70	1.56	0.57	0.45
	mean Doppler velocity (m/sec)	-3.93	8.55	-3.75	8.37	-0.69	1.63	-0.42	0.66
	spectral width (m/sec)	1.62	2.12	2.77	1.88	0.83	1.38	1.27	1.18
CP	mean power (dB)	-220.82	19.33	-10.75	6.14	-238.90	12.56	-10.82	7.29
	mean Doppler velocity (m/sec)	38.88	11.80	4.92	9.49	38.13	9.72	3.10	5.04
	spectral width (m/sec)	3.50	1.90	18.86	6.40	3.48	1.88	16.94	5.73
cMMSE	mean power (dB)	-0.96	2.17	0.14	0.70	-1.52	2.00	-0.30	0.44
	mean Doppler velocity (m/sec)	0.05	1.58	0.01	0.17	0.02	0.86	0.01	0.16
	spectral width (m/sec)	1.53	2.11	1.46	1.41	0.75	1.11	0.66	0.32

Note: A bias of mean power is that a difference between an estimated power in dB and an accumulated truth in dB.

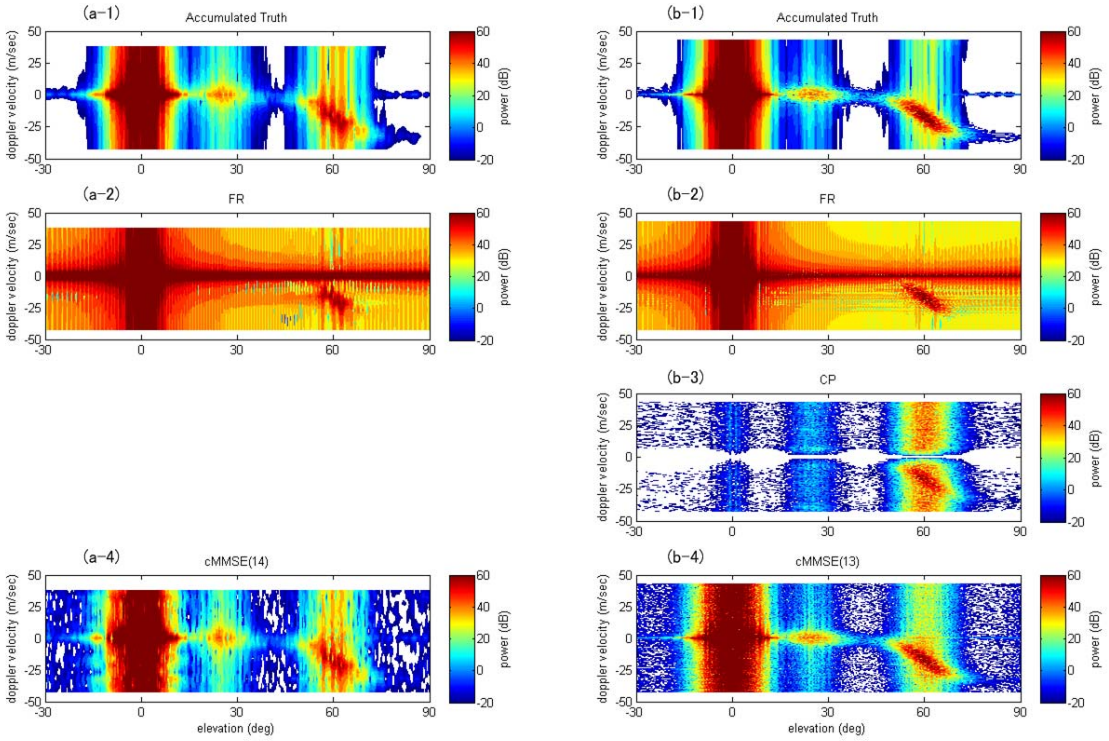

Fig. 5. Examples of elevation – Doppler velocity spectrographs 16 and 256 pulses with anticipated strong ground clutters. In Panels (a-1), (a-2) and (a-4), spectrographs of accumulated truth, FR, and cMMSE are shown. Spectrograph of CP, corresponding to Panel (a-3), is not shown because of the too over underestimation with 16 pulses. Those of accumulated truth, FR, CP, and cMMSE with 256 pulses are shown in Panel (b-1), (b-2), (b-3), and (b-4), respectively.

elevation angles from 13 to 77 deg (indicated by the blue area in Fig. 3), 2) beyond sidelobes of FR in elevation angles from 20 to 30 deg and 55 and 65 deg (indicated by two yellow areas). Estimation accuracies are validated by mean bias errors (mean of differences between estimated powers in dB and accumulated truths in dB) and standard deviations compared with accumulated truth with the use of 256 simulations signals with different random numbers for both the radar signal simulator and additional noise. In Table III, estimation accuracies with 16 and 256 pulses in the two validated regions are summarized. While there are large errors in the blue colored area, FR indicates good estimation accuracies in the yellow colored areas without affections of sidelobes. On the other hand, FR's mean Doppler and spectral width estimates are worse than the other two methods. The reason for this is shown in an example of Doppler spectrograph shown later. CP cannot output valid results with 16 pulses. Since mean power estimates have large negative bias errors less than -200 dB, the other two estimates are no longer worthy of discussion. With 256 pulses, the CP results are improved, and it is clear that CP is not affected by sidelobes. However, CP's mean power estimates have negative biases. This negative bias is suppressed with a greater number of pulses, as stated above. Spectral width estimates of CP have large bias errors and standard deviations, which are not resolved with more pulses. cMMSE results indicate excellent accuracies. Regardless of the number of pulses, cMMSE correctly estimates these three parameters without sidelobes. cMMSE has a bias error of -1.52 dB with 16 pulses in the yellow areas, which is 2.2 times higher than that of FR. Since cMMSE also has a negative bias of -0.3 dB even with 256 pulses in the blue area, cMMSE tends to slightly underestimate mean powers with a large magnitude.

The elevation-Doppler velocity spectrographs shown in Fig. 4 are very helpful for understanding the characteristics of these methods. Panels (a-2) and (b-2) show that signals contaminate each other by their sidelobes in FR. This is why mean Doppler velocity and spectral width estimates are biased even if the large signals do not appear to be contaminated in Panels (a-1) and (b-1) in Fig. 3. Panel (b-3) shows that the CP's Doppler spectrums in every elevation are stretched wider than the accumulated truth of Panel (b-1), which lead to the large biases indicated in Table III. Focusing Doppler velocities around 0 m/sec, spectrums are weakened because high correlations between these signals affect CP's performance. CP's spectrograph with 16 pulses is not shown here because underestimations are too large, as stated above. Compared with them, spectrographs of cMMSE in Panel (a-4) and (b-4) are very similar to those of the accumulated truth in Panels (a-1) and (b-1).

C. Ground Clutter

The PAWR is designed to observe precipitation in urban areas in which it is anticipated that strong ground clutter and its sidelobes significantly contaminate the desired signals. Ground clutter appears at elevations in which ground, trees, or

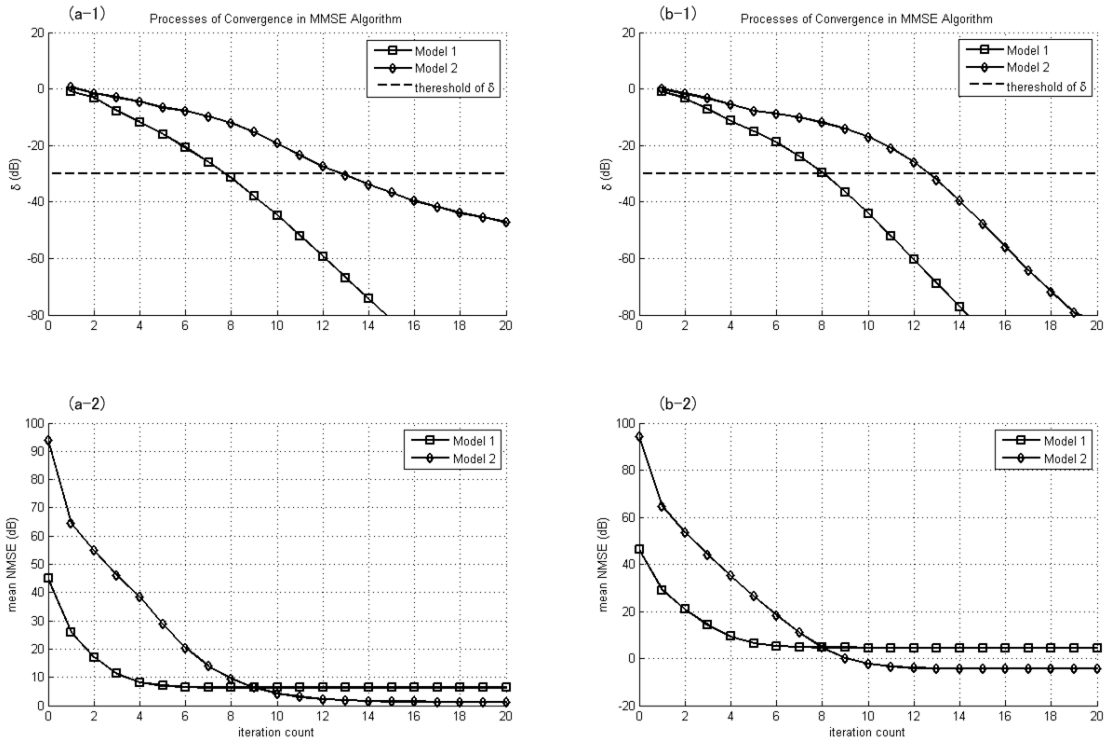

Fig. 6. Convergence processes of the MMSE algorithm. Panel (a-1) shows convergence processes of δi along iteration count, in which square and diamond symbols indicate those for Models 1 and 2 with 16 pulses, respectively, and a black dashed line is the threshold to judge if a solution is converged. Panel (a-2) shows convergence processes of mean NMSE between accumulated truth and MMSE solutions with 16 pulses. Panels (b-1) and (b-2) shows those processes in the case with 256 pulses.

buildings exist in a desired range bin. Furthermore, ground clutter in other range bins around the desired one also should affect the signals by tails of modulated pulses by a receiver band width [23], [24] or their range sidelobes if it's a pulse compression radar [25], [26]. These beam-forming methods never suppress ground clutter itself but can mitigate its sidelobes. Additionally, with strong clutter signals, estimated results of MMSE could be worse because it is obvious that the condition numbers of matrix $\mathbf{R}_x$ is large.

In this section, estimated results are evaluated with the use of the two-cell model, as in the former section, with the addition of ground clutter signals. The ground clutter elements have a mean power of a Gaussian shape whose peak is positioned at 0 deg elevation with about 110 dB peak power. Their mean Doppler velocities and spectral widths are 0 m/sec and 0.2 m/sec, respectively, in all the elevations. This clutter signal is also generated by the radar signal simulator stated above. Spectrographs of the three methods with 16 and 256 pulses are shown in Fig. 5. In this case, FR in Panels (a-2) and (b-2) has sidelobes too large to detect the distributed signals, and CP in Panel (b-3) also has larger underestimations than the no clutter case. cMMSE in Panels (a-4) and (b-4) correctly suppresses the sidelobes of the strong ground clutter and lets the distributed signals appear regardless of the number of pulses. Table III indicates estimated accuracies of cMMSE in this case. Mean biases and standard deviations are calculated estimation results in elevations from 20 to 30 deg and 55 and 65 deg (the two yellow areas). All the parameters are almost the same as Table II.

TABLE IV
NUMBER OF ITERATIONS FOR CONVERGENCE

	L = 16		L = 256	
	Model 1	Model 2	Model 1	Model 2
max	10	20	9	14
min	7	12	8	12
mean	8.68	13.73	8.74	13.01
standard deviation	0.65	1.09	0.44	0.23

D. Convergence of the MMSE Algorithm

It is important to know how to converge solutions in the MMSE iterations and to confirm whether the converge condition for the termination, Eq (25), is correct. Of course, a process of convergence is dependent on distribution of signals. In this section, using the same simulation models as those in Subsections B and C (called Models 1 and 2), convergence processes of the MMSE algorithm are validated. In Fig. 6, examples of convergence processes are shown. Panels (a-1) and (b-1) show convergence processes of δ_i, indicated in Eq. (25), with 16 and 256 pulses, respectively. Corresponding mean NMSEs in each range bin between MMSE(i) and accumulated truth are shown in Panels (a-2) and (b-2). In each case, δ_i and the corresponding mean NMSEs decrease along the iteration count, and the mean NMSEs sufficiently converge when δ_i is under the threshold of -30 dB (see Table I). Table IV

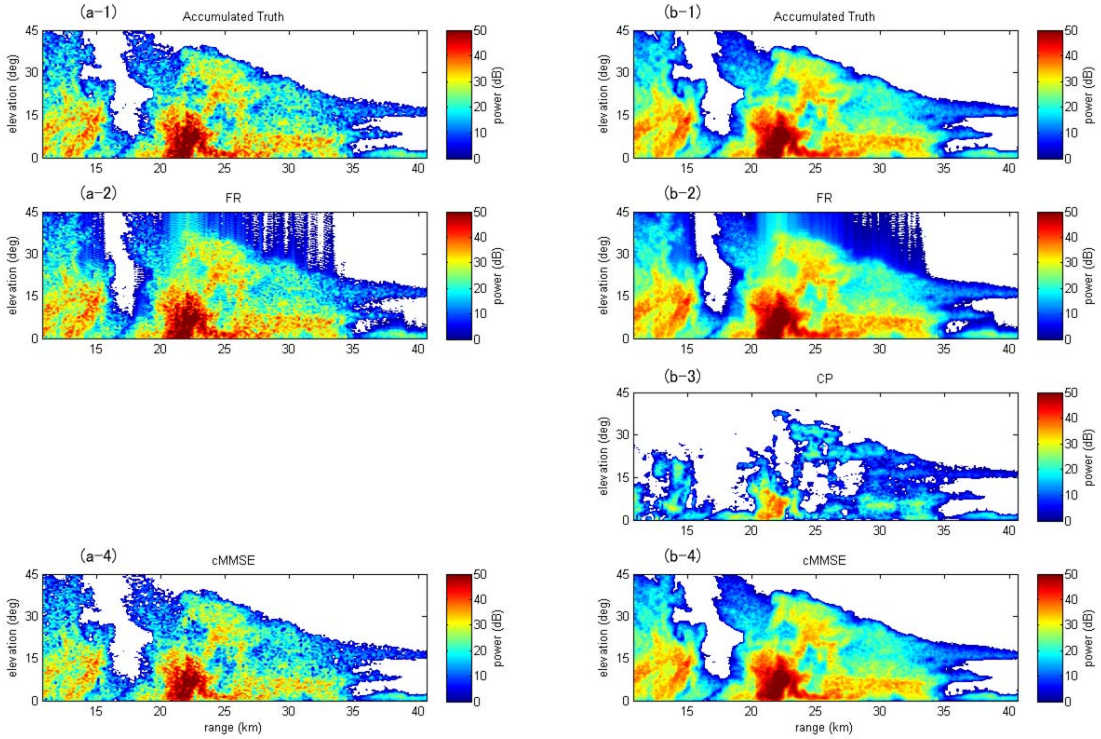

Fig. 7. Range-elevation cross sections of reflectivity in a simulation based on data collected by the CSU-CHILL radar. Panels (a-1), (a-2), and (a-4) are reflectivities with 16 pulses of accumulated truth, FR, and cMMSE, respectively. Panel (a-3), which is for CP, is not shown because of its extreme underestimation. Those with 256 pulses are in Panels (b-1) through (b-4).

summarizes the number of iteration counts for convergence with 16 and 256 pulses in the two simulation models. The maximum, minimum, mean, and standard deviation of the number of iterations are derived from 256 simulations, as in Subsections B and C. The mean value depends on the models. MMSE converges faster in Model I because the initial solution in Model 2 is farther from truth than Model 1. The simulation with ground clutter with 16 pulses takes the most number of interactions, and the algorithm reached the maximum number of 20 in 4 of 256 simulations.

IV. Application to the CSU-CHILL Measurements

To describe the performance of these methods, a simulation with precipitation data observed on the CSU-CHILL radar was carried out. The CSU-CHILL radar data provide more realistic profile of precipitation, which is not described in the former simulations (for example, large gradients of reflectivity). Additionally, the estimated results indicate which parts of precipitation structure MMSE works better than other methods in. In an RHI observation on Aug. 1, 2011, reflectivity, mean Doppler velocity, spectral width, etc., were obtained in elevations from -0.07 to 45.33 deg (almost 0.15 deg spacing) with -3-dB beam width of 1 deg. Linear interpolation for each obtained parameter gave precipitation profiles with 0.1 deg spacing. Time-series data with 16 and 256 pulses were generated from these parameters by the radar signal simulator. Fig. 7 shows a range-elevation cross section of reflectivity of accumulated truth, FR, CP, and cMMSE with 16 and 256 pulses. This comparison clearly illustrates that cMMSE correctly detects precipitation profiles. It is very difficult to visually find out differences between accumulated truth (Panels (a-1) and (b-1)) and cMMSE (Panels (a-4) and (b-4)). In FR (Panels (a-2) and (b-2)), precipitation is not observed correctly beyond and below strong echoes, especially in ranges from 20 to 35 km, due to high sidelobes. The results of cMMSE indicate that cMMSE contributes to accurate detection of precipitation. One important advantage of cMMSE is that echo tops are clearly identified. In addition, precipitation structures at low altitudes, in which precipitation has more variability due to interactions with the ground surface, are accurately estimated. It is also clear that anvils in ranges from 35 to 40 km are separately described. In this data, CP's performance (Panel (b-3)) is worse than the former simulations because input Doppler velocities are similar along elevations (Panel (a-3) is not shown because of large underestimation as above). Even in a convective rain like this sample, signals from precipitation are highly correlated and, therefore, CP needs a larger number of pulses. It is also shown here that the cMMSE performance is not dependent on the number of pulses.

V. Conclusion

At present we are developing a phased array weather radar (PAWR) to rapidly scan and finely detect hazardous weather phenomena with spatial resolution of 500 m 3-D mesh and

temporal resolution of 10 sec per volume scan. The main concept of this radar is fan beam transmission and sharp beam reception, which drastically accelerate scan speed. Transmitting and receiving beams are formed by analog phase shift and DBF, respectively. To accomplish this style of observation, it is very important to suppress beam sidelobes because the sidelobes of the two-way antenna pattern are almost two times higher than formal sharp beam transmission and reception. Though many digital beam-forming methods to suppress sidelobes have been proposed, almost all of them are designed for target detection. Not only sidelobe suppression but also estimation accuracy is necessary in weather radar observation. In this paper, a beam-forming method based on MMSE is proposed, and its performance for the distributed targets such as precipitation is evaluated.

Because the MMSE beam forming proposed in [16] does not have any constraint for minimization, the power of formed mainlobe is unstable. In this paper, estimation accuracies are improved by the addition of a gain constraint as in [20] and a convergence condition based on NMSE. Performances are validated by numerical simulation. Generated data simulate precipitation, which has narrow band random signals whose Doppler spectrum is a Gaussian shape with a center frequency and spectral width corresponding to motions of radiated precipitation particles. Simulation results indicate that the MMSE algorithm adaptively suppresses sidelobes and correctly estimates power, mean Doppler velocity, and spectral width. It is also confirmed that those performances are superior to FR and CP, which are traditionally applied to phased array radars for distributed targets. Though CP also suppresses sidelobes of undesired signals, it needs a large number of pulses to avoid underestimations. In contrast, MMSE shows excellent performance even with 16 pulses; therefore, MMSE is appropriate for the PAWR, which obtains around 16 pulses per single direction to scan rapidly. In 256 simulations of two precipitation cells with 16 pulses, mean biases of mean power, mean Doppler velocity, and spectral width are -0.96 dB, 0.05 m/sec, and 1.53 m/sec, and standard deviations of mean power, mean Doppler velocity, and spectral width are 2.17 dB, 1.58 m/sec, and 2.11 m/sec, respectively (beyond additional nose level). Additionally, it is anticipated that strong ground clutter contaminates the desired distributed signals because the PAWR is designed to be installed in urban area. In numerical simulations with strong ground clutter, MMSE shows performance as good as simulations without ground clutter. Though the MMSE method never suppresses ground clutter itself, sidelobes of ground clutters, which significantly contaminate in high elevation angles, are mitigated. This helps a following ground clutter filter work well. Simulations with data obtained by the CSU-CHILL radar were also carried out. Though this evaluation with data obtained in the CSU-CHILL radar does not assure that the algorithms perform as well as with real data obtained in the PAWR, MMSE shows excellent performance even with these radar signals data representing precipitation more realistically. These results indicate that this MMSE approach can be applied to pulse compression weather radars for ranging with high resolution [27], [28], [29]. In range signal processing, signals outside of processing window often contaminate estimation results more than in DBF processing. This problem could be solved by applying the MMSE approach with an extended processing window, as shown in [17].

For practical use, many kinds of additional noises such as calibration errors in each element, mutual coupling between elements or between an antenna system and a radome, diffraction of a water coated radome, quantization error in digital sampling, and so on, disturbs the signal model, Eq. (1). However, these errors could be solved by applying a modified signal model as indicated in [16]. As a future work, we will carry out these error analyses, which are indicative for designing the PAWR. Also, computational cost is an important issue in practical. Roughly estimating from Eq. (20), the MMSE approach has a computational cost 20 times more than the CP with 20 iterations. As a faster approach instead of some extent of deterioration, a modified MMSE approach has been proposed [19]. We will make a feasibility study about this with the PAWR specification fixed in near future.

ACKNOWLEDGMENT

This work is supported by Toshiba Corporation and the National Institute of Information and Communications Technology (NICT). The authors acknowledge Dr. V. Chandrasekar at Colorado State University, and Pat Kennedy, and Jim George at the CSU-CHILL National Radar Facility for providing the data from the CSU-CHILL radar and for productive discussions. The authors also acknowledge Dr. Toshio Iguchi and Dr. Shinsuke Satoh at NICT for productive discussions.

REFERENCES

[1] D. J. McLaughlin, et al., "Short-Wavelength Technology and the Potential For Distributed Networks of Small Radar Systems," *Bulletin of the American Meteorological Society*, vol. 90, Dec. 2009, pp. 1797–1817.

[2] F. Junyent and V. Chandrasekar, "Theory and characterization of weather radar networks," *J. Atmos. Oceanic. Technol.*, vol. 26, Jul. 2008, pp. 474–491.

[3] D. S. Zrnic, J. M. Kimpel, D. E. Forsyth, A. Shapiro, G. Crain, R. Ferek, J. Heimmer, W. Benner, T. J. McNellis, and R. J. Vogt, "Agile-beam phased array radar for weather observations," *Bulletin of American Meteorological Society*, vol. 88, Nov. 2007, pp. 1753–1766.

[4] F. Junyent and V. Chandrasekar, "The CASA integrated project 1 networked radar system," *J. Atmos. Oceanic. Technol.*, vol. 27, Jul. 2009, pp. 61–78.

[5] J. Wurman and M. Randall, "An Inexpensive, Mobile, Rapid-Scan radar", in *30th Int. Conf. on Radar Meteor. Soc.*, Oct. 2009.

[6] B. Isom et al., "The Atmospheric Imaging Radar (AIR) for High-Resolution Observations of Severe Weather", in *2011 IEEE Radar Conf.*, Kansas City, 2011.

[7] A. L. Pazmany and H. B. Bluestein, "Mobile Rapid-Scanning X-band Polarimetric (RaxPol) Doppler Radar", in *35th Conf. on Radar Meteor.*, Pittsburgh, 2011.

[8] H. B. Bluestein, Michael M. French, Ivan PopStefanija, Robert T. Bluth, and Jeffrey P. Knorr, "A mobile, phased-array Doppler radar for the study of severe convective storms," *Bull. Amer. Meteor. Soc.*, vol. 91, 579 – 600, 2010.

[9] F. Mizutani, M. Wada, T. Ushio, E. Yoshikawa, S. Satoh, and T. Iguchi, "Development of Active Phased Array Weather Radar," in *35th Conf. on Radar Meteor.*, Pittsburgh, 2011.

[10] J. Capon, "High-resolution frequency-wavenumber spectrum analysis," in *Proc. IEEE*, 1969, pp. 1408–1418.

[11] R. D. Palmer, S. Gopalam, T.-Y. Yu, and S. Fukao, "Coherent radar imaging using Capon's method," *Radio Science*, vol. 33, Dec. 1998, pp. 1585–1598.

[12] R. D. Palmer, T-Y. Yu, and P. B. Chilson, "Range imaging using frequency diversity," *Radio Science*, vol. 34, Nov.-Dec. 1999, pp. 1485-1496.
[13] H. Luce, M. Yamamoto, S. Fukao, D. Helal, and M. Crochet, "A frequency domain radar interferometric imaging (FII) technique based on high-resolution methods," *Journal of Atmospheric and Solar-Terrestrial Physics*, vol. 63, Mar. 2001, pp. 221–234.
[14] B. L. Cheong, M. W. Hoffman, R. D. Palmer, S. J. Frasier, and F. J. Lopez-Dekker, "Pulse pair beamforming and the effects of reflectivity field variations on imaging radars," *Radio Science*, vol. 39, Jun. 2004.
[15] B. L. Cheong, M. W. Hoffman, and R. D. Palmer, "Efficient Atmospheric Simulation for High-Resolution Radar Imaging Applications," *J. Atmos. Oceanic. Technol.*, vol. 21, Feb. 2004, pp. 374–378.
[16] S. D. Blunt, T. Chan, and K. Gerlach, "Robust DOA Estimation: The Reiterative Superresolution (RISR) Algorithm," *IEEE Trans. Aerospace and Electronic System*, vol. 47, Jan. 2011, pp. 332–346.
[17] S. D. Blunt and K. Gerlach, "Adaptive pulse compression via MMSE estimation," *IEEE Trans. Aerospace and Electronic System*, vol. 42, Apr. 2006, pp. 572–584.
[18] K. Gerlach and S. D. Blunt, "Radar pulse compression repair," *IEEE Trans. Aerospace and Electronic System*, vol. 43, Apr. 2007, pp. 1188–1195.
[19] S. D. Blunt and T. Higgins, "Achieving real-time efficiency for adaptive radar pulse compression," in *Proc. 2007 IEEE Radar Conf.*, Boston, 2007, pp. 116–121.
[20] T. Higgins, S. D. Blunt and K. Gerlach, "Gain-constrained adaptive pulse compression via an MVDR framework," in *Proc. 2009 IEEE Radar Conf.*, Pasadena, 2009, pp. 1–6.
[21] V. Chandrasekar, V. N. Bringi, and P. Brockwell, "Statistical properties of dual-polarized radar signals," in *Proc. 23rd Conf. on Radar Meteorology.*, Snowmass, 1986, pp. 192–196.
[22] D. S. Zrnic, "Simulation of weatherlike Doppler spectra and signals," *J. Appl. Meteor.*, Vol. 14, Jun. 1975, pp. 619-620.
[23] V. N. Bringi and V. Chandrasekar, *Polarimetric Doppler Weather Radar: Principles and Applications.* Cambridge, U.K.: Cambridge Univ. Press, 2001, pp. 222–232.
[24] R. J. Doviak and D. S. Zrnic, *Doppler Radar and Weather Observations.* San Diego, CA: Academic, 1993, pp. 72–82.
[25] M. Skolnik, *Radar Handbook.* New York, NY: McGraw-Hill, 2008, pp. 8.1–8.44.
[26] P. J. Peebles, *Radar Principles.* New York, NY: John Wiley & Sons, 1998, pp. 287–354.
[27] T. Mega, K. Monden, T. Ushio, K. Okamoto, Z. Kawasaki, and T. Morimoto, "A low-power high-resolution broad-band radar using a pulse compression technique for meteorological application," *IEEE Geosci. Remote Sens. Lett.*, vol. 4, Jul. 2007, pp. 392–396.
[28] E. Yoshikawa, T. Ushio, Zen Kawasaki, T. Mega, S. Yoshida, T. Morimoto, K. Imai, and S. Nagayama "Development and initial observation of high-resolution volume-scanning radar for meteorological application," *Trans. IEEE Geosci. Remote Sens.*, vol. 48, Aug. 2010, pp. 3225–3235.
[29] D V. Chandrasekar, M. Schwaller, M. Vega, J. Carswell, K .V. Mishra, R. Meneghini, and C. M. Nguywn, "Scientific and engineering overview of the NASA Dual-Frequency Dual-Polarized Doppler Radar (D3R) system for GPM Ground Validation," in *Proc. 2010 IEEE International Geosci. And Remote Sens. Symposium*, Honolulu, 2010, pp. 1308–1311.

Eiichi Yoshikawa (M'09) received B.S. degree in Aerospace Engineering from Osaka Prefecture University, Japan, in 2005 and M.S. and Ph.D. degrees in Division of Electrical, Electric and Information Engineering from Osaka University, Japan, in 2008 and 2010, respectively. He was with Osaka University and Colorado State University, CO, USA as a post-doctoral researcher in 2011. Currently, he is with Japan Aerospace Exploration Agency (JAXA). His research specialties are radar-based remote sensing, signal processing, and atmospheric science.

Tomoo Ushio (M'00) received the B.S, M.S., and Ph.D. degree in electrical engineering from Osaka University in 1993, 1995, 1998, respectively. He was with the Global Hydrology and Climate Center, Huntsville AL USA as a Postdoctorate Researcher from 1998 to 2000. In 2000, he joined the Department of Aerospace Engineering, Osaka Prefecture University. After being an assistant professor at Osaka Prefecture University, in 2006, he joined the Division of Electrical, Electric and Information Engineering, Osaka University Japan where he is currently an associate professor. His research specialties are radar-based remote sensing, passive and active remote sensing of atmosphere from space-born platforms, and atmospheric electricity.

Zen Kawasaki (M'72) received B.S., M.S., and Dr. Eng. Degrees in communications engineering from Osaka University in 1973, 1975, and 1978, respectively. In 1989, he joined the Department of Electrical Engineering, Osaka University. At present, he is a professor of the Division of Electrical, Electronic and Information Engineering. He is the dean advisor of Egypt Japan University of Science and Technology (E-JUST). His research mainly concerns the electromagnetic compatibility and atmospheric electricity. He is the fellow of IEE Japan, and the president of International Commission on Atmospheric Electricity (ICAE).

Satoru Yoshida received the B.S degree in Physics from Kobe University in 2001 and the M.S. degree in Communications Engineering from Osaka University in 2003. He received the Ph.D. degree in Electrical, Electronic, and Information Engineering in 2008 from Osaka University. After he was a research fellow of the Japan Society for the Promotion of Science (JSPS Research Fellow) from 2008 to 2009, he joined the Frontier Research Base for Global Young Researchers, Osaka University where he is currently an assistant professor. His research mainly concerns atmospheric electricity.

Takeshi Morimoto received the B.S and M.S. degrees in electrical engineering and the Ph.D. degree in communications engineering from Osaka University in 2000, 2002, and 2005, respectively. In 2005, he joined the same department as a faculty member. After being an associate professor at Osaka University, in 2012, he joined the Department of Electric and Electronic Engineering, Faculty of Science and Engineering, Kinki University, Osaka Japan where he is currently an associate professor. His main interests are in remote sensing and relative engineering.

Fumihiko Mizutani received the B.S degree in science from Kyushu University in 2001, and the M.S degree in science from Nagoya University in 2003. In 2003, he joined Toshiba Corporation where he is currently a specialist. His work mainly concerns weather observation and forecast system.

Masakazu Wada received the B.S and M.S. degrees in electrical engineering from Musashi Institute of Technology in 1992 and 1994, respectively. He received the Ph.D. degree in Electrical, Electronic Engineering in 1997 from Osaka University. In 1997, he joined Toshiba Corporation where he is currently a chief specialist. His work mainly concerns weather observation and forecast system.